

T-FAKE: Synthesizing Thermal Images for Facial Landmarking

Philipp Flotho^{*1} Moritz Piening^{*2} Anna Kukleva³ Gabriele Steidl²

Abstract

Facial analysis is a key component in a wide range of applications such as security, autonomous driving, entertainment, and healthcare. Despite the availability of various facial RGB datasets, the thermal modality, which plays a crucial role in life sciences, medicine, and biometrics, has been largely overlooked. To address this gap, we introduce the T-FAKE dataset, a new large-scale synthetic thermal dataset with sparse and dense landmarks. To facilitate the creation of the dataset, we propose a novel RGB2Thermal loss function, which enables the transfer of thermal style to RGB faces. By utilizing the Wasserstein distance between thermal and RGB patches and the statistical analysis of clinical temperature distributions on faces, we ensure that the generated thermal images closely resemble real samples. Using RGB2Thermal style transfer based on our RGB2Thermal loss function, we create the T-FAKE dataset, a large-scale synthetic thermal dataset of faces. Leveraging our novel T-FAKE dataset, probabilistic landmark prediction, and label adaptation networks, we demonstrate significant improvements in landmark detection methods on thermal images across different landmark conventions. Our models show excellent performance with both sparse 70-point landmarks and dense 478-point landmark annotations. Our code and models are available at <https://github.com/phf1ot/tfake>.

1 Introduction

Functional thermal imaging is an acquisition modality with growing importance in many areas from life sciences over medicine to biometrics. Due to the close relation of body temperature with physiological states, thermal imaging of faces emerged as an important tool for screening infectious diseases [45, 40, 4] and for the analysis of neurocognitive and affective states [21]. As a consequence, there exists a growing need for thermal images with annotated facial landmarks. However, in contrast to RGB images, annotated data for thermal images of faces is still rarely available. For example, the largest thermal datasets with facial landmark annotations contain

^{*}Equal contribution.

¹Systems Neuroscience & Neurotechnology Unit, Faculty of Medicine, Saarland University & htw saar

²Institute of Mathematics, Technische Universität Berlin

³Max Planck Institute for Informatics, Saarland Informatics Campus

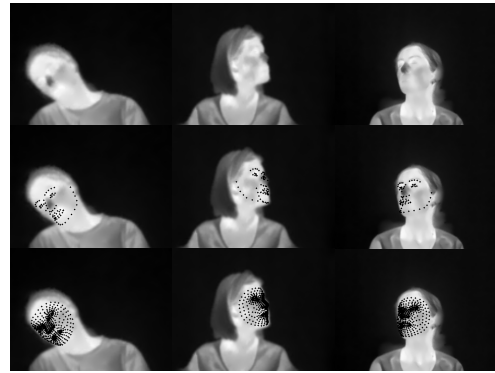


Figure 1: Predictions of 70 (middle) and 478 (bottom) point facial landmarks on the challenging CHARLOTTE dataset which are estimated accurately by training a model with our synthetic data.

only tens to hundreds of individuals [29, 12, 43, 3], while the largest datasets for face detection for RGB images reached the mark of a million faces (of more than 500k individuals) with the MegaFace benchmark already in 2016 [24]. Moreover, large synthetic RGB datasets, like FAKE [52] appeared to be valuable for landmark detection training.

Generally, the detection of facial landmarks is an important downstream task for facial analysis. These 2D coordinates of corresponding points across faces are part of methods, e.g., for alignment of faces to extract regions of interest [53], the animation of 3D avatars [35], motion magnification [14, 13] or deep-fakes [46]. The most common convention for facial landmark annotations uses 68 points across the face and face boundary, see, e.g. [48]. Even though the 68-point convention remains challenging for thermal images [42, 37], the importance of dense landmarkers with more than 300 points has been demonstrated [52, 53, 35].

Faces in thermal images share structural similarities with RGB images. However, temporally varying environmental factors such as temperature and rain droplets, and physiological factors such as blood perfusion changes and vascular details lead to much higher variability in the appearance of faces within individuals [20]. Sweating, flushing, or outdoor rain can result in time-dependent texture changes. Features that are very stable in RGB images such as the contrast of the nose and the eyes can become inverted when the nose or the face is cooled down. Due to the structural similarities, landmarkers trained on RGB datasets were also used under specific thermal imaging conditions [12]. However, they show high failure rates and produce imprecise landmark predictions on challenging thermal images. Up to now, there exist only a few sparse thermal landmark detection methods [29, 37, 43, 33, 32], and we are unaware of a dense thermal or a multimodal RGB+Thermal landmark system. In this paper, we aim to address this gap by introducing the T-FAKE dataset, the first large-scale synthetic thermal dataset featuring both sparse and dense landmarks for facial analysis. We propose to thermalize a synthetic RGB dataset using our novel RGB2Thermal loss function, which comprises three key components: i) a supervised data term that

controls the generation of thermal faces based on a small subset of RGB-thermal pairs, ii) a Wasserstein distance term that aligns the patch distributions of the generated synthetic thermal images with those of real thermal images, and iii) a term incorporating prior information on clinical temperature statistics for different facial regions. To validate the quality of our T-FAKE dataset, we employ a probabilistic landmark prediction method by minimizing the negative log-likelihood function of the landmarks which are assumed to follow a Gaussian distribution as proposed in [53]. Moreover, by introducing a learnable adapter between different landmark conventions, we unify various methods and datasets for evaluation.

We thoroughly evaluate the landmark prediction method trained on our T-FAKE dataset on the established RGB dataset 300W [48] and the challenging thermal dataset CHARLOTTE [3], which includes controlled modulation of environmental parameters such as pose and resolution. Our model demonstrates superior performance on the thermal landmark prediction benchmark compared to previous methods while maintaining performance on the RGB images comparable to state-of-the-art RGB methods. Fig. 1 illustrates the performance of our model for sparse and dense landmarking. In summary, we provide the following contributions:

- The first large-scale facial synthetic thermal dataset T-FAKE with sparse and dense landmark annotations;
- A novel RGB2Thermal loss to facilitate thermal image synthesis overcoming limited lab-recorded training data;
- Training of the up-to-date first dense thermal landmarker and a state-of-the-art multimodal RGB+Thermal sparse landmarker in combination with highly structured benchmarking across different landmark conventions and modalities.

2 Related Work

Facial RGB landmarking. The most widely used annotation convention defines 68-point landmarks which are available for many facial alignment

Dataset name	Year	DS available	Model available	Landmarks	Size (F/S)	Distance (cm)
Aachen[29]	2018	✓	✓	68	2935/90	90
ARL-MMFD [54]	2019	(request)	✗	6	?/111	250, 500, 750
DRIVE-IN [12]	2021	✗	✗	68 and 468	?/436	~80-150
ARL-VTF [43]	2021	✗	✗	68	?/395	210
TFW [32]	2022	✓	✓	5	9982/147	100-?
SF-TL54 [33]	2022	✓	✓	54	2556/142	100
CHARLOTTE [3]	2022	✓	✗	73 (43 profile)	7684/10	100-660
T-FAKE (ours)	2024	✓	✓	70 and 468	200k/2k	~80-150

Table 1: Comparison of thermal landmark datasets. Number of frames (F) and number of subjects (S) are indicated as well as distance to the camera if known. Unavailable data are marked by a question mark.

datasets [27, 55, 6]. Sometimes points on the eye or other details are additionally added [52, 3]. While an in-depth review of facial RGB landmarking is beyond the scope of this work, we introduce those that are relevant to thermal landmarking methods. Kazemi et al. [23] introduced a traditional computer vision method for landmark prediction that is still widely used via the dlib library [25]. Kowalski et al. [30] proposed the deep alignment network (DAN) which uses convolutional neural networks and iteratively refines landmark predictions. Around the same time, Bulat et al. [6] proposed the facial alignment network (FA). Both methods predict heat maps of landmark positions from which coordinates are computed. Explicit integration of uncertainty quantification into a deep landmark prediction model via the LUVLi loss has been proposed by Kumar et al. [31]. In recent years, the quality of image annotation became a limiting factor of modern algorithms which led to the emergence of synthetic data with high-quality ground truth [39]. Wood et al. [52, 53] trained landmarkers on synthetic data that outperform traditional approaches and proposed the FAKE dataset with 100k frames of 2k individual faces.

Thermal landmarking. Many tailored approaches for thermal landmarking use similar architectures as RGB landmarkers and are mainly developed alongside the publication of new datasets, see Table 1. Kuzdeuov et al. [32] released the TFW dataset with a total number of 9982 images from 147 subjects annotated with 5 facial landmarks and bounding boxes and trained YOLOv5 networks for landmark predic-

tion. The SF-TL54 dataset [33] consists of 54 landmarks and 2556 frames of 142 subjects and has been used for landmark prediction with a dlib and a U-net model. Kopaczka et al. [29] also use a dlib model for their AACHEN dataset with annotated 2935 images of 90 subjects and 68-point landmarks. A highly structured dataset is the CHARLOTTE thermal face dataset with 10 subjects and 10k images by Ashrafi et al. [3], who annotated their dataset with 72-point landmarks. In contrast to these publicly available datasets, datasets with limited or no public availability include the the ARL-VTF dataset [43] (500k frames of 395 subjects) and a dataset recorded in SARS-CoV-2 drive-in stations (DRIVE-IN) [12] (six minutes recordings at 50Hz of 436 subjects). The authors of the DRIVE-IN dataset found that a stack of pre-processing functions already leads to a good performance of existing RGB landmark models on thermal images. Similarly, Poster et al. [44] proposed to use transfer learning on a siamese DAN to improve thermal landmark prediction with RGB facial landmarks. Mallat et al. [37] used RGB2Thermal image translation (‘thermalization’), active appearance models, and deep alignment networks of RGB datasets for thermal landmark prediction. In contrast to the previous work, our dataset contains thermal images of 2k individuals that are annotated with sparse 70 as well as dense 478 point landmarks.

Thermalization. In addition to thermal landmark datasets, various datasets of paired and aligned thermal and RGB images without annotations exist. These can be employed for the training of thermal-

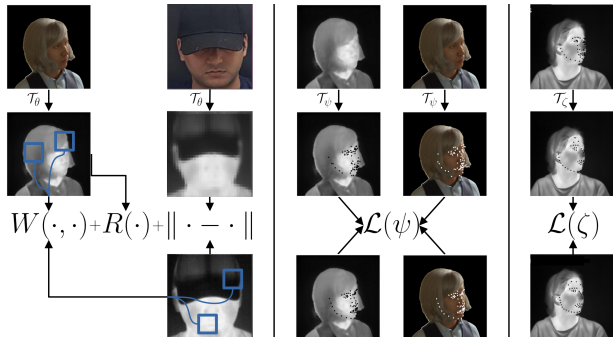


Figure 2: Three steps of our training pipeline (models and their loss functions): 1. thermalization network \mathcal{T}_θ with loss (1) - (3). 2. landmark prediction network \mathcal{T}_ψ with (6). 3. landmark adaptation network \mathcal{T}_ζ with (7). We show black dots for thermal landmarks and white dots for RGB landmarks. Note the landmark adaptation on the forehead in the last step.

ization models. Mallat et al. thermalized facial images by minimizing a perceptual loss [37] using the VIS-TH dataset [36]. Similarly, generative adversarial networks (GANs) have been used for thermalization [54, 20] using the NCKU-VTF [20] dataset and the ARL-MMDF [54] dataset containing facial image data. In contrast to the limited public availability of these two datasets, a publicly available dataset with paired facial images is the multi-modal disguise *Sejong face database* (SEJONG) with 100 subjects, 15 disguise variations and 4849 RGB+Thermal image pairs by Cheema and Moon [7]. Thermalization of general scenes has been achieved by Kniaz et al. [26] with a modified Pix2Pix GAN, where they used the publicly available ThermalWorld dataset with 5098 image pairs displaying various object classes. In contrast to previous works, we employ a semi-supervised RGB2Thermal loss that incorporates a semantic segmentation to improve generalization.

3 T-FAKE Dataset

Recently, the success of landmarkers trained solely on the synthetic facial landmarking dataset FAKE [52] has demonstrated the potential of synthetic data for landmarking. We aim to transfer this success

story to the largely overlooked thermal domain and the multimodal setting by introducing our synthetic thermal landmarking dataset T-FAKE featuring 2k unique subjects.

In particular, we train a semi-supervised image translation model for the thermalization of RGB images using real and synthetic data. To account for variations in the data in terms of poses, hairstyles, and expressions, we employ a semi-supervised loss.

3.1 Thermalization

To generate our large-scale synthetic T-FAKE dataset, we propose a thermalization framework. First, we train our network in a semi-supervised manner based on training pairs of RGB+Thermal images $(\mathbf{X}_{\text{RGB}}, \mathbf{X}_{\text{T}}) = (X_{\text{RGB}}^n, X_{\text{T}}^n)_{n=1}^N$ from the lab-recorded SEJONG dataset. Further, we use the synthetic RGB images from FAKE $\mathbf{X}_{\text{FAKE}} = (X_{\text{FAKE}}^m)_{m=1}^M$ for which no thermal counterpart exists. Indeed the thermalization of these data appears to be difficult due to the large differences between real-world lab-recorded and synthetic in-the-wild data when facing thermalization tasks. For RGB2Thermal translation, we optimize a U-net [47] T_θ by minimizing the loss function

$$\mathcal{L}(\theta) := \frac{1}{N} \sum_{n=1}^N \|T_\theta(X_{\text{RGB}}^n) - X_{\text{T}}^n\|_2^2 \quad (1)$$

$$+ \lambda_W W(T_\theta(\mathbf{X}_{\text{FAKE}}), \mathbf{X}_{\text{T}}) \quad (2)$$

$$+ \lambda_R \frac{1}{M} \sum_{m=1}^M R(T_\theta(X_{\text{FAKE}}^m)), \quad \lambda_W, \lambda_R > 0. \quad (3)$$

This loss allows us to simultaneously train a domain-adaptive image translation model from paired and unpaired data. The first summand (1) penalizes the deviation of the generated thermal image from the true one and serves as a reconstruction loss for known image pairs. The second summand (2) exploits the Wasserstein distance on the patch distribution of thermalized FAKE images and natural thermal images. This style loss ensures that a generated image displays the thermal image statistics. To be more precise, recall that the squared Wasserstein-2 distance

\mathcal{W}_2^2 between empirical measures $\mu = \frac{1}{K} \sum_{k=1}^K \delta_{x_k}$ and $\nu = \frac{1}{L} \sum_{l=1}^L \delta_{y_l}$ is given by

$$\mathcal{W}_2^2(\mu, \nu) := \inf_{\pi \in \Pi} F(\pi) := \sum_{k=1}^K \sum_{l=1}^L \|x_k - y_l\|^2 \pi_{k,l}, \quad (4)$$

where Π denotes the set of non-negative $K \times L$ matrices which rows and columns sum up to $1/K$ and $1/L$, respectively. Calculation with this distance requires solving costly optimization problems. As a remedy, the entropy-regularized Wasserstein distance

$$\mathcal{W}_{2,E}^2(\mu, \nu) := \inf_{\pi \in \Pi} \left\{ F(\pi) + \lambda_E \sum_{k=1}^K \sum_{l=1}^L \pi_{k,l} \log(\pi_{k,l}) \right\}$$

with some (small) regularization $\lambda_E > 0$ has been proposed [9]. The new formulation and the resulting gradients can efficiently be calculated via the Sinkhorn algorithm [11, 41]. To use this loss for thermal translation, we focus on the patch distributions of the generated and real images. For that purpose, we now extract (overlapping) image patches $P_i X := X[i_1 : i_1 + s, i_2 : i_2 + s]$, $i = (i_1, i_2) \in I$ of size $s \times s$ and consider the empirical measures generated by the patch distributions of $T_\theta(\mathbf{X}_{\text{FAKE}})$,

$$\mu_{\text{FAKE}} := \frac{1}{N} \frac{1}{|I|} \sum_{n=1}^N \sum_{i=1}^{|I|} \delta_{P_i(T_\theta(X_{\text{FAKE}}^n))},$$

and similarly μ_{T} from X_{T} . Now we penalize in (2) the term

$$W(T_\theta(\mathbf{X}_{\text{FAKE}}), \mathbf{X}_{\text{T}}) := \mathcal{W}_{2,E}^2(\mu_{\text{FAKE}}, \mu_{\text{T}}). \quad (5)$$

During training, we apply a *multiscale approach* by applying this regularizer over multiple image scales and summing over the results. As a result, the patch statistics of downscaled images are incorporated into the empirical loss. The proposed patch distribution matching-based regularization was inspired by its application in related tasks such as image reconstruction [1, 41], style transfer [34], texture reconstruction [18, 2], and image translation [22].

Finally, the distribution of temperature across different regions of the face and body are well-studied

[50, 8], e.g., warmer areas around the eyes, colder scalp hair and glasses blocking thermal heat. Thus, the third summand (3) incorporates such knowledge about the expected temperature in different facial areas. To be specific, we make use of a given semantic segmentation of the synthetic dataset of the image $\mathbf{X}_{\text{F-RGB}}$ into pixels corresponding to 18 regions S_i , e.g., ‘background’, ‘nose’, ‘headwear’ and so on. Moreover, let T_i be the average temperature of the hardcoded reference temperatures in the region S_i based on measurements presented in empirical studies [8, 50, 3]. Then, we compute

$$R(T_\theta(\mathbf{X}_{\text{FAKE}})) = \sum_{m=1}^M \sum_{i=1}^{18} \omega_i (\overline{S_i(T_\theta(X_{\text{FAKE}}^m))} - T_i)^2,$$

where the weights ω_i are proportional to the region sizes and $\overline{S_i}$ is the mean temperature in the i -th region. Note that facial temperatures depend on the environmental conditions. Hence, we train T_θ two times with two different reference temperature sets to simulate ‘cold’ and ‘warm’ environmental conditions. The different regularizers are visualized in Fig. 2 (left) and the segmentation masks are shown in Fig. 3 (bottom).

Predictions of the normalized temperature with our model compared to a model without regularization are shown in Fig. 3. The advantages of our regularization in a domain-adapted setting are clearly visible. The use of regularization reduces image artifacts. The patch regularizer (2) promotes natural texture synthesis and because of our segmentation regularizer (3) temperature differences between facial areas are more pronounced. Hence, our method allows for the adaptation of images with shadows, various skin colors, and distinctive facial expressions. In particular, such features may be underrepresented in facial thermal imaging datasets recorded in lab conditions. Note that the resulting domain adaptation needs for synthetic data and the access to ground truth segmentations differentiates our task from the thermalization tasks in [26, 54, 37, 20].



Figure 3: Frames from the FAKE dataset [52] before (first row) and after thermalization without any regularization (second row) and our domain-adaptive model (third row). The last row displays the segmentation masks with gray levels which are proportional to the reference temperature values used in regularizer (3). The first three images exemplify the ‘cold’ setup with colder noses and the last two the ‘warm’ setup with warmer noses.

3.2 The Dataset

Having trained T_θ , we use it to thermalize the FAKE dataset which results in the thermal dataset T-FAKE. For each thermal condition, the dataset contains 100k images featuring 2k unique subjects. Each image is available in a simulated ‘cold’ and a ‘warm’ environment adding up to 200k images. This number of frames and subjects surpasses the numbers in other thermal landmarking datasets [29, 54, 12, 43, 32, 33, 3] known to the authors. In contrast to thermal landmarking datasets with a fixed distance between the subjects and the camera [29, 43, 33], the distance varies within an estimated range of 80cm to 150cm for the T-FAKE dataset. Moreover, the synthesized images are based on facial scans with a wide range of age and ethnicity and a balanced number of people identifying as male or female [52]. In addition to the original ground truth sparse landmark annotations, we add dense annotations by transferring Mediapipe [35] predictions for the FAKE to the T-FAKE dataset. This makes our dataset the first densely annotated

thermal landmarking dataset. While we found many of the large thermal landmarking datasets to be non-public [54, 12, 43], our complete dataset with both thermal conditions and annotations is available for download. In combination with the original FAKE dataset, we can train multimodal facial landmarkers jointly on RGB and thermal images as described in the next section. Table 1 displays a detailed comparison between thermal landmarking datasets

4 Facial Landmarking

Learning with synthetic images has proven to be very useful in facial landmarking [54, 52, 53]. Based on the proposed T-FAKE and the original FAKE dataset, we can thus train a supervised thermal or multimodal landmark prediction model for thermal and RGB images using synthetic data only. Moreover, we can adapt our model to new annotation conventions by training a small-scale label adaptation model. The data flow for these two models is visualized in Fig. 2.

4.1 Landmark Prediction

We apply the construction in [53] and learn a landmark prediction model through probabilistic landmark regression from given paired data $(X^j, \mathbf{y}_j)_{j=1}^J$, where $X^j \in \text{FAKE} \cup \text{T-FAKE}$ and $\mathbf{y}_j := (y_l^j)_{l=1}^L$, $y_l^j \in \mathbb{R}^2$ are the corresponding L landmarks. We learn a network T_ψ mapping from the space of images to the space of L -fold two-dimensional Gaussian distributions $(\mathcal{N}(\mu_l, \sigma_l I_2))_{l=1}^L$. Here we employ a MobileNet V2 architecture for landmark prediction [49]. Recalling that the Gaussian distribution $\mathcal{N}(\mu, \sigma I_2)$ has the *negative log-likelihood function*

$$-\log p(y|\mu, \sigma) = \log(2\pi\sigma^2) + \frac{\|\mu - y\|_2^2}{2\sigma^2},$$

the authors of [53] proposed to learn the network $T_\psi := (T_\psi^1, T_\psi^2)$ with $X \mapsto (\boldsymbol{\mu}, \boldsymbol{\sigma}^2)$, where $\boldsymbol{\mu} = (\mu_l)_{l=1}^L \in (\mathbb{R}^2)^L$ and $\boldsymbol{\sigma}^2 = (\sigma_l^2)_{l=1}^L \in \mathbb{R}^L$ by mini-

mizing the loss function

$$\mathcal{L}(\psi) := \sum_{l=1}^L \left(\sum_{j=1}^J \log T_{\psi,l}^2(X^j) + \frac{\|T_{\psi,l}^1(X^j) - y_l^j\|_2^2}{2T_{\psi,l}^2(X^j)} \right). \quad (6)$$

During training, we clip $T_{\psi,l}^2 \geq \varepsilon > 0$ to avoid numerical instability due to too small variances. The first sum controls the location accuracy and the second one the uncertainty prediction. Having learned the network T_ψ , it produces not only the expected values μ of the corresponding landmarks, but also a measure for its uncertainty σ^2 .

4.2 Label Adaptation

A common approach that is especially crucial for synthetic trained data is label adaptation [52, 53]. It allows us to adapt to different landmark conventions between the training dataset and an evaluation dataset. Given two sequences $(\hat{\mathbf{y}}_k, \mathbf{y}_k)_{k=1}^K$ with predicted landmarks $\hat{\mathbf{y}}_k := (\hat{y}_k^l)_{l=1}^{\hat{L}} \in \mathbb{R}^{2\hat{L}}$, and with ground truth landmarks $\mathbf{y}_k := (y_k^l)_{l=1}^L \in \mathbb{R}^{2L}$ with possibly $\hat{L} \neq L$, we aim to train a third label adaptation model $T_\zeta : \mathbb{R}^{2\hat{L}} \rightarrow \mathbb{R}^{2L}$. Here, we use the loss

$$\mathcal{L}(\zeta) = \frac{1}{K} \sum_{k=1}^K \|T_\zeta(\hat{\mathbf{y}}_k) - \mathbf{y}_k\|_1. \quad (7)$$

Since we deal with low-dimensional data, we use a simple multi-layer fully connected perceptron with 5 layers for this task, see supplementary material for details.

5 Experiments

In this section, we present details of our final implementation and our benchmarking pipeline. Note that we clamp the temperature of all thermal images between 20 °C and 40 °C for all experiments and visualizations.

5.1 Implementation Details

Thermalization. We train on the RGB+Thermal SEJONG dataset recorded in lab conditions and the

large-scale synthetic FAKE dataset featuring in-the-wild RGB images. We train on a resolution of 256×256 . For the patch-based regularizers, we use a patch size of 8. We disregard the background by excluding synthetic patches based on the ground truth background segmentation and completely black real patches. For our multi-scale approach, we sum the regularizer over 5 scales with a downsampling factor of 0.5. Furthermore, facial temperatures depend on the surrounding temperature.

Thus, we train a ‘warm’ and a ‘cold’ model with different reference temperature values for the segmentation-based regularizers, see Fig. 3. For data augmentation, we use the same random rotations and cropping for the natural RGB and thermal images. Moreover, we apply random color changes, blurring, and shadow augmentations [38] exclusively to the natural RGB images. Next, we apply random rotations and cropping for the synthetic RGB images. Here, we also fill holes in the original ‘glasses’ segmentation masks showing outlines of the frame only to highlight transparent, but heat-blocking glass or plastic, see Fig. 3 (bottom right). Lastly, we replace the original background with a black background based on the known semantic segmentation. We apply our two models to the FAKE dataset at the original 512×512 resolution to generate the T-FAKE dataset. This results in the up-to-date largest thermal landmarking dataset with 200k images of 2k unique subjects and two thermal settings, see Table 1.

Landmarker. We simultaneously train our landmark prediction model using a sparse 70-point and dense 468-point landmark convention with an image size of 224×224 on our new T-FAKE thermal dataset and the original FAKE RGB dataset. Additionally, we include random landmark positions on a texture dataset [16] as negative examples into the dataset to increase the learned uncertainty σ^2 on images without faces. Due to the limited, public availability of the dense ground truth in the FAKE dataset [52], we use the 468-point predictions of the MediaPipe model for the synthetic RGB images as our dense ground truth dense annotations. We make use of spatial augmentations, including random shear, rotations, resiz-

ing, and cropping to allow the landmarker to learn a large variation of face orientations without the need for a dedicated face detector. Furthermore, we employ Gaussian blur, color jitter, and global pixel offset for thermal images during training. On thermal images, we fill in the background with random textures from the texture dataset [16]. During inference, we use a multi-scale sliding window evaluation to generalize our model to varying image sizes. We downsample iteratively with a factor of 0.75 until the height or the width is smaller than 224. For each image scale, we run our model on sliding windows of size 224×224 with a stride of 20. For our final landmark prediction, we pool all predictions and use the landmark with the smallest predicted standard deviation across all scales and all sliding windows.

Label Adaptation. Our label adaptation network is trained solely on the two-dimensional landmark predictions and ground truth annotations of a training split of a benchmark dataset and not on the images. This dataset is later excluded from the final evaluation. We do not use the predicted standard deviation at this stage. Again, we use random rotations and shear transformations during training.

Evaluation Metrics for Landmarking. We report the *normalized mean error* (NME) [52, 48, 56] for evaluation, i.e., the mean absolute error (MAE) normalized with an image-dependent constant to account for varying image sizes. Often, normalization is performed by the distance between the outermost eye landmarks (NME Interocular) [52, 48]. However, the CHARLOTTE benchmark dataset contains many examples with side profile views where only one of the eyes is visible. Therefore, we use the average height and width of the bounding box around the face for normalization [56] (NME W/H). Apart from the NME, we report the failure rates for each of the reference methods. The failure rate is the percentage of frames where no faces could be found. Frames without recognized faces are not included nor weighted in the NMEs. The method of rejection varies for each landmarker. We use vanilla parameters except for MediaPipe [35], where we set the minimal detection confidence to 0.01. For our method, we evaluate it i) on all frames without failure rate and ii) on

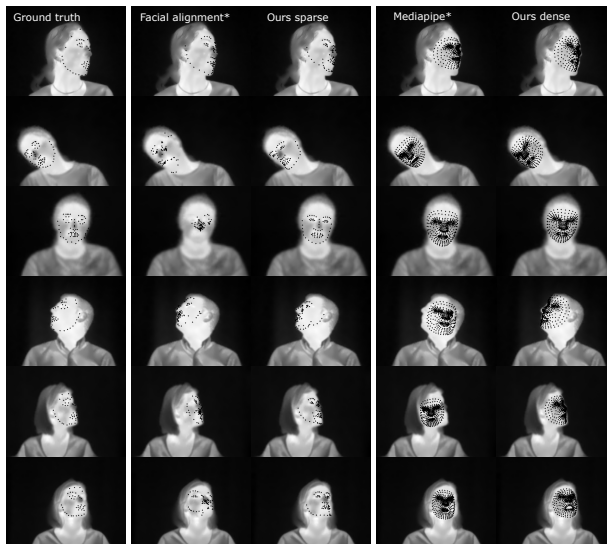


Figure 4: Results on examples from the CHARLOTTE dataset [3] of FA and Mediapipe with the full pre-processing stack and our models without label adaptation. While the RGB methods can handle some challenging poses, they produce broken landmarks on certain difficult images.

all frames where the average uncertainty scores σ_l of the predicted landmarks l , $1 \leq l \leq L$, is less than $\bar{\sigma} = 6 \times 10^{-4}$.

5.2 Benchmark Datasets for Landmarking

To compare thermal performance, we use the CHARLOTTE dataset due to its high variability in resolution, pose, and background temperature. The dataset is annotated with either 72 landmarks for frontal images or 43 landmarks for lateral images. The 43-point landmarks represent the visible landmarks in profile pictures with our information on orientation. The dataset contains a total of 7685 annotated frames with different resolutions with a minimal one of around 70x60. For evaluation, we split the CHARLOTTE dataset based on image size and perspective. The CHARLOTTE High condition contains all images larger than the median image width of 200 pixels and CHARLOTTE Low all smaller images. The condition CHARLOTTE Side includes

Metric	Method	Charlotte High	Charlotte Low	Charlotte Side	Charlotte Front	Charlotte Full
NME	Aachen [28]	0.1677	0.2405	0.2942	0.1731	0.2054
	3FabRec [5]	0.2862	0.3195	0.1810	0.4259	0.3033
	3FabRec*	0.2646	0.3272	0.1921	0.4015	0.2967
	Mediapipe [17]	0.1900	0.2745	0.2879	0.1865	0.2262
	Mediapipe*	0.1400	0.2621	0.1838	0.2164	0.2023
	FA [6]	0.1070	0.2790	0.1222	0.2508	0.1875
	FA*	0.1007	0.2207	0.1075	0.2123	0.1593
	TFW [32]	0.0787	0.1249	0.0701	0.1311	0.1012
	SF-TL54 U-Net [33]	0.2476	0.3134	0.1757	0.3596	0.2829
	SF-TL54 Dlib [33]	0.2159	0.2174	0.1365	0.2741	0.2167
	Ours dense ($\bar{\sigma} < \infty$)	0.0805	0.1285	0.0846	0.1258	0.1050
	Ours ($\bar{\sigma} < \infty$)	0.0740	0.1346	0.0684	0.1420	0.1051
	Ours ($\bar{\sigma} < 6 \times 10^{-4}$)	0.0729	0.1139	0.0628	0.1219	0.0923
Failure rate (%)	Aachen [29]	49.32	48.72	72.85	25.15	49.01
	Mediapipe [35]	25.05	46.85	50.09	22.40	36.25
	Mediapipe*	12.80	14.07	24.97	1.92	13.45
	FA [6]	12.95	27.43	21.71	19.07	20.39
	FA*	0.83	10.45	4.75	6.80	5.77
	TFW [32]	13.14	21.55	19.26	15.66	17.46
	SF-TL54 U-NET / Dlib [33]	29.29	22.57	38.16	13.50	25.84
	Ours ($\bar{\sigma} < 6 \times 10^{-4}$)	1.63	16.45	9.15	9.34	9.25

Table 2: Results on the CHARLOTTE dataset. Pre-processing with the full pre-processing stack for RGB landmarks is indicated by *. The low resolution (3434 frames) and high resolution (3250 frames) are defined by the median image width of 200 pixels. We denote the confidence threshold with $\bar{\sigma}$. Note that we include all predictions for $\bar{\sigma} < \infty$ and 3FabRec resulting in a failure rate of 0 by design.

Method	300W		Regularization		FID
	NME W/H	NME Interocular	$\lambda_R = 0, \lambda_W = 0$	$\lambda_R = 0, \lambda_W = 0.01C$	$\lambda_R = 1, \lambda_W = 0$
3FabRec [5]	0.0376	0.0646	$\lambda_R = 1, \lambda_W = 0$	$\lambda_R = 1, \lambda_W = 0.01C$	0.3325 ± 0.0039
FA [6]	0.0618	0.1083			0.3139 ± 0.0035
Ours	0.0330	0.0577			0.2719 ± 0.0054
Ablation Study					
GB	0.0303	0.0523			0.2666 ± 0.0037

Table 3: Comparison of RGB performance of our method. We trained the label adaptation on 300 random samples of the combined W300 outdoor and indoor scenes (600 images) and evaluated the remaining images.

all images with profile annotations (43 landmarks), and CHARLOTTE Front contains all frontal faces (73 landmarks). In addition, we evaluate on the established RGB landmark dataset 300W [48] to verify RGB landmark prediction performance. It uses the classical 68-point convention. Here, we crop images to the pre-defined bounding boxes around each face for our evaluation. The average image resolution is about 290 pixels.

Table 4: Influence of the regularizers on the thermalization. The parameter λ_W corresponds to the impact of the patch-based regularizer (Eq. (2)) and λ_R corresponds to the segmentation-based regularizer (Eq. (3)). We use $C = (5 \cdot 8^2)^{(-1)}$.

5.3 Comparison to State-of-the-Art

We compare the performance of our landmarker trained on our full synthetic datasets against the state-of-the-art models on the CHARLOTTE dataset. Here, we include not only relevant thermal landmark detection systems but also RGB landmark detection systems. A previous study has shown that the performance of RGB landmarkers on thermal images can be significantly boosted by applying a stack of unlearned linear filters before prediction [12]. Consequently, the application of this pre-processing stack

Metric	Method	Charlotte High	Charlotte Low	Charlotte Side	Charlotte Front	Charlotte Full
	RGB	0.1055	0.2675	0.1241	0.2534	0.1887
NME	RGB*	0.0933	0.2682	0.1312	0.2348	0.1824
	Thermal Only	0.0832	0.1334	0.0677	0.1503	0.1090

Table 5: Ablation results on the CHARLOTTE dataset. Pre-processing with the full pre-processing stack for RGB landmarks is indicated by *. Here, we do not exclude low-confidence images. Hence, we report the NME on all images without failure rate

of linear filters allows us to include RGB landmarks in our benchmark and to draw a fair comparison beyond task-specific thermal landmarks. Because the CHARLOTTE dataset uses its own landmark convention, we use label adaptation for all methods for the image evaluation. We train each label adaptation model with a 1000-image training split on CHARLOTTE similar to [52] and exclude the training split from the final evaluation. Note that this approach allows us to include our sparse model and our dense model in the evaluation. To benchmark the RGB performance of the multimodal model, we evaluate our sparse model predictions against state-of-the-art RGB sparse landmarks on the 300W dataset.

CHARLOTTE performance. The NME performance as well as the failure rates of the different methods varies drastically for the different CHARLOTTE splits. We observe the lowest performance across the landmarks on the Front condition, followed by the low-resolution images. The FA and Mediapipe RGB methods show a performance that is comparable with the SF-TL54 and Aachen thermal landmarks. Using a pre-processing stack [12], they consistently outperform them on the High condition in terms of NME and on Full, Front, Low and Side in terms of failure rate. Our model achieves state-of-the-art performance for sparse thermal landmarking across all different conditions. The only model with comparable performance is TFW which, however, only predicts a set of 5 landmarks. While the NME of TFW is slightly lower than our method for $\bar{\sigma} < \infty$ for Low, Front, and Full, our method outperforms TFW on all dataset splits in terms of NME and failure rate for $\bar{\sigma} < 6 \times 10^{-4}$. These results are presented in Table 2 and examples are visualized in Fig. 4.

300W performance. Additionally, we evaluate the

RGB models on the 300W dataset in Table 3. Our model, trained on a combination of thermal and RGB facial images, demonstrates competitive performance on RGB images, being outperformed only by the original model trained exclusively on RGB data. The overall performances are consistent with the literature [52].

5.4 Thermalization Ablation Study

We ablate our different regularizers in Eq. (1)-(3) using the *Fréchet Inception Distance* (FID) [19]. The FID measures image distribution similarity between a real and a synthetic set of images based on an Inception v3 [51] model pre-trained on ImageNet [10]. For our evaluation, we report the average FID between the complete SEJONG dataset and twenty equal-sized samples from the FAKE dataset. Here, we use the SEJONG dataset as a reference thermal dataset to evaluate the similarity of differently thermalized images to true thermal images. We thermalize each sample with i) our model without regularization, ii) our model with patch-based regularization (Eq. 2) only, iii) our model with segmentation-based regularization (Eq. 3) only, and iv) our final model. All models are trained with the same setup and we randomly choose the ‘warm’ or the ‘cold’ variant for each image. Table 4 shows the average FIDs and the standard deviations. We see that the segmentation-based regularizer leads to a large boost in perceptual similarity and that the patch-based regularizer leads to a smaller boost. The combination of both regularizers gives the best result and confirms the effectiveness of our RGB2Thermal loss.

5.5 Landmarking Ablation Study

To study the impact of our thermal data, we additionally report the CHARLOTTE results of our landmarker trained with i) RGB images only and ii) thermal images only. Again, we use label adaptation for all variations. Table 5 shows the results. Training with the T-FAKE dataset significantly improves the accuracy of thermal landmarking across all conditions. In addition, multimodal training with the FAKE and T-FAKE datasets leads to better thermal landmarking performance than training only with the T-FAKE dataset. Moreover, we ablate our RGB performance on 300W by testing the model trained on RGB images only, see Table 3. Here, we see a slight drop in performance caused by multimodal training. Nevertheless, our multimodal model still outperforms FA [6] and 3FabRec [5].

6 Conclusion

To overcome data limitations in thermal landmarking, we established a semi-supervised RGB2Thermal image translation method. Using patch-based and segmentation-based regularization, we ensured the generalization of our thermalizer to the synthetic FAKE dataset. We employed this model to generate the up-to-date largest thermal landmarking dataset, the T-FAKE dataset. By training a probabilistic landmarker with the T-FAKE dataset, we established the up-to-date first dense thermal landmarker and a state-of-the-art RGB+Thermal sparse landmarker. We tested these landmarkers with strict benchmarking by including established thermal and RGB methods and using label adaptation for each benchmarked method. Our work shows that synthetic data is sufficient for the training of thermal landmarkers and can be done on multiple imaging modalities.

7 Acknowledgements

This study has partially been funded by the Federal Ministry of Education and Research (BMBF, grant numbers 13N15753 and 13N15754). M.P. acknowledges funding from the German Research Founda-

tion (DFG) within the GRK2260 BIOQIC project 289347353. The authors acknowledge HPC resources support with hardware funded by the DFG within project 469073465. The authors would like to thank Daniel J. Strauss for discussions and Mayur Bhamborae and Pascal Hirsch for technical support.

References

- [1] Fabian Altekrüger, Alexander Denker, Paul Hagemann, Johannes Hertrich, Peter Maass, and Gabriele Steidl. PatchNR: Learning from very few images by patch normalizing flow regularization. *Inverse Problems*, 39(6):064006, 2023. 5
- [2] Fabian Altekrüger and Johannes Hertrich. WPPNets and WPPFlows: The power of Wasserstein patch priors for superresolution. *SIAM Journal on Imaging Sciences*, 16(3):1033–1067, 2023. 5
- [3] Roshanak Ashrafi, Mona Azarbayjani, and Hamed Tabkhi. Charlotte-ThermalFace: A fully annotated thermal infrared face dataset with various environmental conditions and distances. *Infrared Physics and Technology*, 124:104209, 2022. 2, 3, 5, 6, 8, 15, 18, 19
- [4] D. Bitar, A. Goubar, and J.-C. Desenclos. International travels and fever screening during epidemics: A literature review on the effectiveness and potential use of non-contact infrared thermometers. *Eurosurveillance*, 14(6):19115, 2009. 1
- [5] Bjoern Browatzki and Christian Wallraven. 3fabrec: Fast few-shot face alignment by reconstruction. In *CVPR*, 2020. 9, 11
- [6] Adrian Bulat and Georgios Tzimiropoulos. How far are we from solving the 2d & 3d face alignment problem? (and a dataset of 230,000 3d facial landmarks). In *CVPR*, pages 1021–1030, 2017. 3, 9, 11
- [7] Usman Cheema and Seungbin Moon. Sejong face database: A multi-modal disguise face database. *Computer Vision and Image Understanding*, 208:103218, 2021. 4, 15
- [8] Andrija Ćosić, Igor Jovanović, Ivana Kostić, Miona Andrejević-Stošović, Dragan Krasić, and Dragan Mančić. Temperatures of different face regions of healthy people measured by a thermal camera. *Serbian Journal of Electrical Engineering*, 19(1):33–43, 2022. 5
- [9] Marco Cuturi. Sinkhorn distances: Lightspeed computation of optimal transport. *NIPS*, 26, 2013. 5

- [10] Jia Deng, Wei Dong, Richard Socher, Li-Jia Li, Kai Li, and Li Fei-Fei. Imagenet: A large-scale hierarchical image database. In *CVPR*, pages 248–255. IEEE, 2009. 10, 15
- [11] Jean Feydy, Thibault Séjourné, François-Xavier Vialard, Shun-ichi Amari, Alain Trounev, and Gabriel Peyré. Interpolating between optimal transport and MMD using Sinkhorn divergences. In *AISTATS*, pages 2681–2690. PMLR, 2019. 5, 15
- [12] Philipp Flotho, Mayur J Bhamborae, Tobias Grün, Carlos Trenado, David Thinnies, Dominik Limbach, and Daniel J Strauss. Multimodal data acquisition at sars-cov-2 drive through screening centers: Setup description and experiences in saarland, germany. *Journal of Biophotonics*, 14(8):e202000512, 2021. 2, 3, 6, 9, 10, 17, 19
- [13] P. Flotho, C. Heiss, G. Steidl, and D.J. Strauss. Lagrangian motion magnification with double sparse optical flow decomposition. *Frontiers in Applied Mathematics and Statistics*, 9:1164491, 2023. 2
- [14] Philipp Flotho, Cosmas Heiß, Gabriele Steidl, and Daniel J Strauss. Lagrangian motion magnification with landmark-prior and sparse pca for facial microexpressions and micromovements. In *Annual International Conference of the IEEE Engineering in Medicine & Biology Society*, pages 2215–2218. IEEE, 2022. 2
- [15] V. Fomin, J. Anmol, S. Desroziers, J. Kriss, and A. Tejani. High-level library to help with training neural networks in pytorch. <https://github.com/pytorch/ignite>, 2020. 16
- [16] M. Godi, C. Joppi, A. Giachetti, F. Pellacini, and M. Cristani. Texel-att: Representing and classifying element-based textures by attributes. In *BMVC*, 2019. 7, 8
- [17] Ivan Grishchenko, Artsiom Ablavatski, Yury Kartynnik, Karthik Raveendran, and Matthias Grundmann. Attention mesh: High-fidelity face mesh prediction in real-time. *CVPR Workshops*, 2020. 9
- [18] Johannes Hertrich, Antoine Houdard, and Claudia Redenbach. Wasserstein patch prior for image superresolution. *IEEE Transactions on Computational Imaging*, 8:693–704, 2022. 5
- [19] Martin Heusel, Hubert Ramsauer, Thomas Unterthiner, Bernhard Nessler, and Sepp Hochreiter. Gans trained by a two time-scale update rule converge to a local Nash equilibrium. *NIPS*, 30, 2017. 10
- [20] T.-H. Ho, C.-Y. Yu, T.-Y. Ko, and W.-T. Chu. The NCKU-VTF Dataset and a multi-scale thermal-to-visible face synthesis system. In *International Conference on Multimedia Modeling*, pages 463–475. Springer, 2023. 2, 4, 5
- [21] Stephanos Ioannou, Vittorio Gallese, and Arcangelo Merla. Thermal infrared imaging in psychophysiology: Potentialities and limits. *Psychophysiology*, 51(10):951–963, 2014. 1, 19
- [22] Phillip Isola, Jun-Yan Zhu, Tinghui Zhou, and Alexei A Efros. Image-to-image translation with conditional adversarial networks. In *CVPR*, pages 1125–1134, 2017. 5
- [23] V. Kazemi and J. Sullivan. One millisecond face alignment with an ensemble of regression trees. In *CVPR Workshops*, pages 1867–1874, 2014. 3
- [24] Ira Kemelmacher-Shlizerman, Steven M Seitz, Daniel Miller, and Evan Brossard. The MegaFace benchmark: 1 million faces for recognition at scale. In *CVPR*, pages 4873–4882, 2016. 2
- [25] Davis E. King. Dlib-ml: A machine learning toolkit. *Journal of Machine Learning Research*, 10:1755–1758, 2009. 3
- [26] Vladimir V Kniaz, Vladimir A Knyaz, Jiri Hladuvka, Walter G Kropatsch, and Vladimir Mizginov. Thermalgan: Multimodal color-to-thermal image translation for person re-identification in multispectral dataset. In *ECCV Workshops*, 2018. 4, 5
- [27] Martin Koestinger, Paul Wohlhart, Peter M Roth, and Horst Bischof. Annotated facial landmarks in the wild: A large-scale, real-world database for facial landmark localization. In *ICCV Workshops*, pages 2144–2151. IEEE, 2011. 3
- [28] Marcin Kopaczka, Lukas Breuer, Justus Schock, and Dorit Merhof. A modular system for detection, tracking and analysis of human faces in thermal infrared recordings. *Sensors*, 19(19):4135, 2019. 9
- [29] Marcin Kopaczka, Raphael Kolk, Justus Schock, Felix Burkhard, and Dorit Merhof. A thermal infrared face database with facial landmarks and emotion labels. *IEEE Transactions on Instrumentation and Measurement*, 68(5):1389–1401, 2018. 2, 3, 6, 9
- [30] M. Kowalski, J. Naruniec, and T. Trzcinski. Deep alignment network: A convolutional neural network for robust face alignment. In *CVPR Workshops*, pages 88–97, 2017. 3
- [31] Abhinav Kumar, Tim K Marks, Wenxuan Mou, Ye Wang, Michael Jones, Anoop Cherian, Toshiaki Koike-Akino, Xiaoming Liu, and Chen Feng. Luvli face alignment: Estimating landmarks’ location, uncertainty, and visibility likelihood. In *CVPR*, pages 8236–8246, 2020. 3

- [32] Askat Kuzdeuov, Dana Aubakirova, Darina Koishigarina, and Huseyin Atakan Varol. Tfw: Annotated thermal faces in the wild dataset. *IEEE Transactions on Information Forensics and Security*, 2022. [2](#), [3](#), [6](#), [9](#), [18](#)
- [33] A. Kuzdeuov, D. Koishigarina, D. Aubakirova, S. Abushakimova, and H. A. Varol. Sf-tl54: A thermal facial landmark dataset with visual pairs. In *IEEE/SICE International Symposium on System Integration*, pages 748–753. IEEE, 2022. [2](#), [3](#), [6](#), [9](#)
- [34] Arthur Leclaire and Julien Rabin. A stochastic multi-layer algorithm for semi-discrete optimal transport with applications to texture synthesis and style transfer. *Journal of Mathematical Imaging and Vision*, 63(2):282–308, 2021. [5](#)
- [35] Camillo Lugaresi, Jiuqiang Tang, Hadon Nash, Chris McClanahan, Esha Uboweja, Michael Hays, Fan Zhang, Chuo-Ling Chang, Ming Yong, Juhyun Lee, et al. Mediapipe: A framework for perceiving and processing reality. In *CVPR Workshops*, 2019. [2](#), [6](#), [8](#), [9](#), [18](#)
- [36] Khawla Mallat and Jean-Luc Dugelay. A benchmark database of visible and thermal paired face images across multiple variations. In *International Conference of the Biometrics Special Interest Group*, pages 1–5. IEEE, 2018. [4](#)
- [37] Khawla Mallat and Jean-Luc Dugelay. Facial landmark detection on thermal data via fully annotated visible-to-thermal data synthesis. In *IJCB*, pages 1–10. IEEE, 2020. [2](#), [3](#), [4](#), [5](#)
- [38] Osama Mazhar and Jens Kober. Random shadows and highlights: A new data augmentation method for extreme lighting conditions. *arXiv preprint arXiv:2101.05361*, 2021. [7](#)
- [39] Pietro Melzi, Ruben Tolosana, Ruben Vera-Rodriguez, Minchul Kim, Christian Rathgeb, Xiaoming Liu, Ivan DeAndres-Tame, Aythami Morales, Julian Fierrez, Javier Ortega-Garcia, et al. Frcsyn-ongoing: Benchmarking and comprehensive evaluation of real and synthetic data to improve face recognition systems. *Information Fusion*, 107:102322, 2024. [3](#)
- [40] E. Y.-K. Ng. Is thermal scanner losing its bite in mass screening of fever due to sars? *Medical Physics*, 32(1):93–97, 2005. [1](#)
- [41] M. Piening, F. Altekrieger, J. Hertrich, P. Hagemann, A. Walther, and G. Steidl. Learning from small data sets: Patch-based regularizers in inverse problems for image reconstruction. *arXiv preprint arXiv:2312.16611*, 2023. [5](#)
- [42] Domenick Poster, Shuowen Hu, Nasser Nasrabadi, and Benjamin Riggan. An examination of deep-learning based landmark detection methods on thermal face imagery. In *CVPR Workshops*, pages 0–0, 2019. [2](#)
- [43] Domenick Poster, Matthew Thielke, Robert Nguyen, Srinivasan Rajaraman, Xing Di, Cedric Nimpa Fondje, Vishal M Patel, Nathaniel J Short, Benjamin S Riggan, Nasser M Nasrabadi, et al. A large-scale, time-synchronized visible and thermal face dataset. In *WACV*, pages 1559–1568, 2021. [2](#), [3](#), [6](#)
- [44] Domenick D Poster, Shuowen Hu, Nathan J Short, Benjamin S Riggan, and Nasser M Nasrabadi. Visible-to-thermal transfer learning for facial landmark detection. *IEEE Access*, 9:52759–52772, 2021. [3](#)
- [45] B. J. Quilty, S. Clifford, S. Flasche, R. M. Eggo, et al. Effectiveness of airport screening at detecting travellers infected with novel coronavirus (2019-ncov). *Eurosurveillance*, 25(5):2000080, 2020. [1](#)
- [46] Md Shohel Rana, Mohammad Nur Nobil, Beddhu Murali, and Andrew H Sung. Deepfake detection: A systematic literature review. *IEEE Access*, 10:25494–25513, 2022. [2](#)
- [47] Olaf Ronneberger, Philipp Fischer, and Thomas Brox. U-net: Convolutional networks for biomedical image segmentation. In *MICCAI*, pages 234–241. Springer, 2015. [4](#)
- [48] Christos Sagonas, Epameinondas Antonakos, Georgios Tzimiropoulos, Stefanos Zafeiriou, and Maja Pantic. 300 faces in-the-wild challenge: Database and results. *Image and Vision Computing*, 47:3–18, 2016. [2](#), [8](#), [9](#)
- [49] Mark Sandler, Andrew Howard, Menglong Zhu, Andrey Zhmoginov, and Liang-Chieh Chen. Mobilenetv2: Inverted residuals and linear bottlenecks. In *CVPR*, pages 4510–4520, 2018. [6](#)
- [50] Saurabh Sonkusare, Michael Breakspear, Tianji Pang, Vinh Thai Nguyen, Sascha Frydman, Christine Cong Guo, and Matthew J Aburn. Data-driven analysis of facial thermal responses and multimodal physiological consistency among subjects. *Scientific Reports*, 11(1):12059, 2021. [5](#)
- [51] Christian Szegedy, Vincent Vanhoucke, Sergey Ioffe, Jon Shlens, and Zbigniew Wojna. Rethinking the inception architecture for computer vision. In *CVPR*, pages 2818–2826, 2016. [10](#)
- [52] Erroll Wood, Tadas Baltrušaitis, Charlie Hewitt, Sebastian Dziadzio, Thomas J Cashman, and Jamie

- Shotton. Fake it till you make it: face analysis in the wild using synthetic data alone. In *ICCV*, pages 3681–3691, 2021. [2](#), [3](#), [4](#), [6](#), [7](#), [8](#), [10](#), [18](#)
- [53] Erroll Wood, Tadas Baltrusaitis, Charlie Hewitt, Matthew Johnson, Jingjing Shen, Nikola Milosavljevic, Daniel Wilde, Stephan Garbin, Toby Sharp, Ivan Stojiljkovic, Tom Cashman, and Julien Valentin. 3d face reconstruction with dense landmarks. In *ECCV*, 2022. [2](#), [3](#), [6](#), [7](#), [18](#), [19](#)
- [54] H. Zhang, B. S. Riggan, S. Hu, N. J. Short, and V. M. Patel. Synthesis of high-quality visible faces from polarimetric thermal faces using generative adversarial networks. *International Journal of Computer Vision*, 127:845–862, 2019. [3](#), [4](#), [5](#), [6](#)
- [55] Xiangyu Zhu, Xiaoming Liu, Zhen Lei, and Stan Z Li. Face alignment in full pose range: A 3d total solution. *IEEE Transactions on Pattern Analysis and Machine Intelligence*, 41(1):78–92, 2017. [3](#)
- [56] Xiangxin Zhu and Deva Ramanan. Face detection, pose estimation, and landmark localization in the wild. In *CVPR*, pages 2879–2886. IEEE, 2012. [8](#)

In the supplementary material, we give additional information for our method. In section A we provide more details on the thermalization including implementation details and an extended ablation study. In section B, we add details on landmarker and label adaptation implementation. In sections C-F we discuss limitations, the societal impact of our work and provide additional result images of the datasets.

A Thermalization

A.1 Reference Temperature Values

As described in the main document, we train two versions of the thermalizer T_θ to model facial temperature variations under different environmental conditions. For that purpose, we use two sets of reference temperatures, a ‘cold’ and a ‘warm’ condition, for the different facial regions that guide the segmentation-based regularizer. These are presented in Table 6. Thermal facial contrast is increased and overall body temperature is decreased for the ‘cold’ condition in comparison to the ‘warm’ condition which is in line with empirical findings [3].

Segmentation	‘Cold’	‘Warm’
Background, Glasses	<20	<20
Skin	33	35
Nose	31.5	35
Eyes	34	35
Brows	31	34
Ears	32	35
Mouth Interior	35	35
Lips	32.5	35
Neck	34	35
Hair	30	30
Beard	31	32
Clothing	30	32
Headwear, Facewear	28	28

Table 6: Reference temperatures T_i in Celsius for our segmentation-based regularizer (3) for the ‘cold’ and the ‘warm’ setup. Note that our pixel range goes from 20 °C to 40 °C.

A.2 Thermalization Implementation Details

We use a U-Net T_θ with a Resnet34 encoder pre-trained on ImageNet [10] and train it for 10 epochs with SEJONG batches of size 64 and FAKE batches of size 64. Further, we use an Adam optimizer with an initial learning rate of 0.001 which we reduce to 0.0001 after 4 epochs. Based on a random split, we use 80% of the SEJONG data for training and all available FAKE data. Also, we use the *geomloss* [11] implementation for the Wasserstein patch loss with $\lambda_E = 0.1^6$. We normalize the squared error loss $\|\cdot - \cdot\|_2^2$ by dividing with the image dimension, here 256^2 . Based on the 5 scales and patch dimension 8^2 , we set $\lambda_W = 0.01C$ for our final model with the normalization constant $C = (5 \cdot 8^2)^{-1}$. We set $\lambda_R = 1$. Note that the choice of $\lambda_R = 1$ and C are motivated to control the value range. The (normalized) MSE data fidelity term $\|\cdot - \cdot\|_2^2$ which we evaluate on normalized SEJONG images takes values in the range $[0, 1]$ for arbitrary images with pixel range $[0, 1]$ due to dimensional normalization. To have a similar value range for the evaluated FAKE images, the patch-based regularizer W takes values in $[0, 1]$ for $\lambda_W = C$ with arbitrary normalized images. Moreover, the segmentation-based regularizer R also takes values in $[0, 1]$ for such images given arbitrary normalized reference temperature values in $[0, 1]$ for $\lambda_R = 1$.

A.3 SEJONG Dataset

The SEJONG dataset illustrates the impact of various disguises, including glasses, wigs, and fake beards. Each subject in the dataset is presented with different disguises. As a result, it includes a lot of clothing and hairstyle variations. Most participants have a Southeast Asian or Central Asian ethnic background, but people of other ethnicities are included too. The number of participants identifying as male or female is balanced. This makes it an attractive dataset candidate for thermalization training that is supposed to generalize to a large variety of subjects. Due to reasons of data privacy, we refer to the original publication [7] and abstain from showing SEJONG images.

A.4 Extended Thermalization Ablation Study

Given that the regularizers are solely defined for the synthetic images, we fix $\lambda_T = 1$ to ensure that the regularizer is on the same scale as the MSE of the real images and



Figure 5: T-Fake samples with original images (first row), ‘cold’ images’ (second row), and ‘warm’ images’ (third row). Note the diminished contrasts of the noses and the checks.

Regularization	$\lambda_R = 1$	$\lambda_R = 0$
$\lambda_W = 1C$	0.2714 ± 0.0045	0.3139 ± 0.0035
$\lambda_W = 0.1C$	0.2710 ± 0.0042	0.3134 ± 0.0048
$\lambda_W = 0.01C$	0.2666 ± 0.0037	0.3120 ± 0.0043
$\lambda_W = 0$	0.2719 ± 0.0054	0.3325 ± 0.0039

Table 7: Impact of the regularization parameters on the perceptual quality measured with the FID with $C = (5 \cdot 8^2)^{-1}$.

vary λ_W for our ablation. We train all models with the same setup and random seeds. The FID implementation is the default *PyTorch-Ignite* [15] implementation. Here, we extend the ablation study table in the main document which only displays the best result for $\lambda_W = 0.01C$. In particular, we display the results of a grid search for λ_W and λ_R in Table 7. As described in the main document, we calculate the mean FID and its standard deviation for twenty different subsets of the T-FAKE dataset. Moreover, we use the same setup to compare the perceptual quality of the ‘cold’ and the ‘warm’ setup of our final T-FAKE dataset, see Table 8. Figure 5 shows T-FAKE samples with the ‘cold’ and ‘warm’ variants. In addition, we present some samples generated with different regularization configurations in Figure 6 for the ‘cold’ setup and in Figure 7 for the ‘warm’ setup. Here, we can visually see the impact of the different regularizers.

According to the FID, both regularizers have a posi-

Setup	‘Cold’	‘Warm’
FID	0.2637 ± 0.0044	0.2699 ± 0.0078

Table 8: Perceptual comparison of thermal setups ‘cold’ and ‘warm’ using the FID.



Figure 6: Regularization impact on images for ‘cold’ setup: No regularization ($\lambda_W = 0, \lambda_R = 0$), only patch-based ($\lambda_W = 0.001C, \lambda_R = 0$), only segmentation-based ($\lambda_W = 0, \lambda_R = 1$), and final model ($\lambda_W = 0.001C, \lambda_R = 1$) (top to bottom).

tive impact. The segmentation-based regularizer greatly boosts the perceptual quality, while the effect of the patch-based regularizer is smaller. The optimal FID value is obtained for $\lambda_W = 0.01C$ and $\lambda_T = 1$, the parameters of our final model. The perceptual quality of the figures seems in line with the FID. A closer look at the last two rows in both figures shows that the segmentation-based regularizer alone can lead to smoothed facial areas and overly exaggerated differences on the edges of the semantic segmentation. This becomes more apparent for the ‘cold’ setup as it leads to more thermal contrast within the face, see Figure 6. The FID shows only a small difference between the ‘cold’ and ‘warm’ variants. The ‘warm’ variant displays slightly lower FID values. For a visual comparison of the T-FAKE images with real thermal images, we refer to Fig. 8.

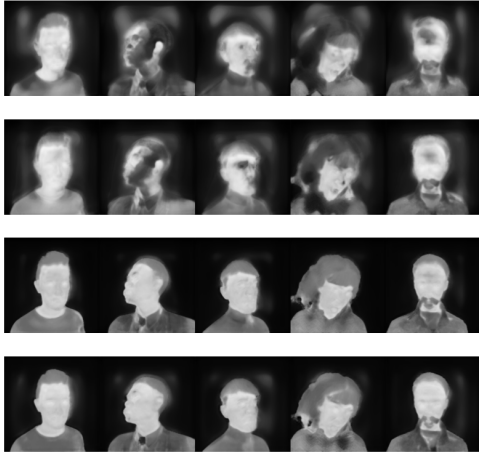


Figure 7: Regularization impact on images for ‘warm’ setup: No regularization ($\lambda_W = 0$, $\lambda_R = 0$), only patch-based ($\lambda_W = 0.001C$, $\lambda_R = 0$), only segmentation-based ($\lambda_W = 0$, $\lambda_R = 1$), and final model ($\lambda_W = 0.001C$, $\lambda_R = 1$) (top to bottom).

B Landmarking

B.1 CHARLOTTE Dataset

The CHARLOTTE dataset contains thermal images with varying thermal conditions, various head positions, and multiple camera distances. Moreover, it contains information about the thermal sensation of the subjects. We refer to Fig. 8 for a visualization of some thermal CHARLOTTE images without landmarks.

B.2 Landmarking Implementation Details

For training the landmarker T_ψ , we finetune a model that has been pre-trained on the original FAKE dataset for the sparse landmarker. For the dense landmarker, pre-training happened on the original FAKE dataset including a first version of the T-FAKE dataset as augmentation with a probability of 0.2. During refinement, thermal images are used with a probability of 0.4 split with equal probability for ‘cold’ and ‘warm’ conditions. We finetune for 100 epochs with a learning rate of 0.0004, Adam optimizer with weight decay, batch size of 512, and OneCycleLR scheduler.



Figure 8: CHARLOTTE image samples with different resolutions, environmental conditions, and subjects.

B.3 Label Adaptation Implementation Details

Label Adaptation was trained for each method on the predictions on all detected faces on a random 1000-image CHARLOTTE split. We train a model T_ζ for 2000 epochs with a learning rate of 0.002, OneCycleLR, and Adam optimizer. As landmark augmentations, we apply random rotation up to 45° as well as random shearing during training. The label adaptation network is a five-layer perceptron with fully connected layers that takes the predicted landmarks together with the resize factor as input. The latter accounts for varying degrees of quantization at different image sizes in the CHARLOTTE ground truth. The label adaptation generally handles even outlier predictions but can also contain fail cases, (see Figure 10).

RGB Model Inference. We use two different pre-processing approaches to include landmarkers solely developed for RGB images in the evaluation. Firstly, gray-value images, where the temperature between 20° and 45° is normalized and, secondly the pre-processing stack proposed in [12]. The pre-processing stack consists of temperature clamping between 20°C and 45°C , unsharp masking with two sets of parameters with and without temperature inversion. The reported landmarks are the averages over all detected faces. This simple pre-processing stack is a simple method for boosting RGB landmarker performance for thermal images [12]. As a

result, we can include RGB landmarks as a baseline for thermal landmarking models.

B.4 Inference Ablation

We analyze the impact of our inference strategy, see Table 9. We compare inference on i.) the complete image scaled to 224×224 (whole image), ii.) followed by refinement on a bounding box computed from the predictions obtained with i.) and finally iii.) with the sliding window approach described in the main document. Method iii.) produces the best results over all images except for Charlotte low, where ii.) performs slightly better while at the same time being also suitable for real-time estimation.

C Large-Scale Visualization

For a large number of T-FAKE samples, we refer to Figures 11 and 12. Here, we simply use the first 128 images based on the numerical naming convention of the original FAKE dataset.

D Thermal Semantic Segmentation Dataset

Note that by design detailed segmentation masks are available for all T-FAKE images. While the training of a semantic segmentation model was out-of-scope for our work, we want to highlight the fact that our dataset can also be used for such training. The possibility of such segmentation training with synthetic data has already been demonstrated by Wood et al. [52].

E Limitations

Thermalization. This work depends on the thermalization of the final renders in the FAKE dataset. The dataset contains very difficult lighting conditions and scene compositions that make it powerful to train landmarkers but also made the thermalization particularly challenging and could only be solved with advanced regularization approaches. Despite a good perceptual result, some T-FAKE images contain artifacts, e.g., black patches on the upper body. Nevertheless, these artifacts remain limited.

Dense Landmarks. In this work, we relied on the ground truth 70-point landmarks of the FAKE dataset [52] and dense Mediapipe [35] annotations. Training with

the original 320-point and 702-point landmarks could further boost accuracy and lead to an even denser landmarker. However, these landmarks are not publicly available. Furthermore, we only evaluate a mobilenet backbone. Performance for difficult poses and face variability could be achieved with denser models [53].

CHARLOTTE. The CHARLOTTE [3] dataset is among the largest datasets with thermal recordings of faces that contain different levels of image quality as well as has a high variability in poses such as side profile pictures and tilting which makes the dataset ideal as a benchmark. However, the annotation uses a non-standard convention where side profile images have a different number of landmarks than frontal faces. Furthermore, landmarks of low-resolution images are quantized and there are examples of shifted ground truth annotations (see Figure 9).

Label Adaptation. We retrain the label adaptation networks for each tested landmarker on its original predictions. Hence, for a given method, a high failure rate on CHARLOTTE means that fewer training images are available for that method. Also, very poor predictions on some of the images such as profile images without failure produce a low quality of adapted landmarks (see Figure 10, TL54 dlib, column 3). It is important to note that the label adaptation does not use visual information from the benchmark dataset to translate landmarks. However, the same individuals were present in both the test and the training dataset splits which might allow the network to learn the facial statistics of individuals. This might give an advantage to landmarkers with only a few landmarks, e.g., TFW [32] (see Figure 10, TFW). The high 68-point landmark performance of TFW on the CHARLOTTE thermal data does not necessarily mean that this generalizes and the advantage of increasing the number of predicted landmarks has been demonstrated for RGB images [53].

F Societal Impact Statement

An increasing number of risks are associated with collecting and using biometric information, such as (thermal) facial images. As for collecting such information in general, biometric datasets contain information that could be misused. Biometric applications, such as facial recognition or landmarking technology, may have internal biases and may display higher error rates for certain populations than for others in terms of, e.g., ethnicity, gender, or age. The use of synthetic data can be very helpful for such

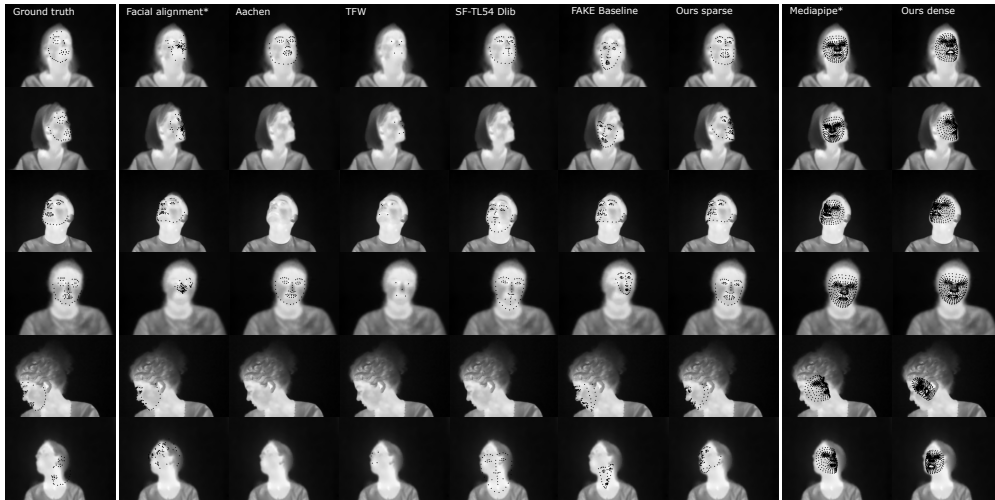


Figure 9: Results on examples from the **CHARLOTTE** dataset [3] with different RGB and thermal predictors and our models. For images without landmarks, no faces were detected. The performance of RGB methods can be greatly improved when the images are inverted or sharpened indicated by *. The first column shows the limitations in the CHARLOTTE ground truth: profile annotation convention for frontal views (1st row), quantization artifacts for low-resolution images (4th row), and translated annotations (last row).

Method	Charlotte High	Charlotte Low	Charlotte Side	Charlotte Front	Charlotte Full
Sliding window ($\bar{\sigma} < \infty$)	0.0740	0.1346	0.0684	0.1420	0.1051
Refined bounding box ($\bar{\sigma} < \infty$)	0.0847	0.1329	0.0696	0.1494	0.1095
Whole image ($\bar{\sigma} < \infty$)	0.1091	0.1868	0.0842	0.2139	0.1490

Table 9: Different strategies for landmark computation. The final results are estimated with sliding windows similar to [53], however, we achieved comparable results when computing the landmarks on input images rescaled to 224×224 . Here, we do not exclude high-uncertainty images and evaluate all images without failure rate, i.e., $\bar{\sigma} < \infty$.

challenges as it allows for explicit control of dataset biases and a decreased need for open-source biometric personal information. Nevertheless, facial recognition technologies can be misused for surveillance purposes and criminal activities. We hope that our research is not employed with malicious intent. Therefore, we strongly encourage the legislative regularization of face recognition and face analysis applications.

Nevertheless, we want to point out the advantages of facial analysis in the thermal domain since this domain is nearly invariant to lighting conditions and inherently difficult to falsify. Highly accurate thermal landmarks can offer security and authentication benefits to society. The computation of reliable thermal landmarks is a key technology for medical screening of various diseases and remote assessment of the physiological and psychophysiological state of humans [12]. Contactless screening for

infectious diseases has the potential to reduce environmental impact as well as to increase security through up-scaled screening in pandemic or endemic scenarios. This, however, requires a detailed understanding of the limitations of such methods and can otherwise result in a false sense of security or discrimination against false positive users and dense landmarks offer a way to better interpret imaged temperatures from the face and pinpoint contributions from distinct facial areas.

The availability of dense thermal imaging to the biomedical research communities promises new applications and new scientific insights from highly accurate temperature analysis of the face. Traditionally, studies involving thermal imaging of faces are analyzed within a semi-automated pipeline which would require manual region-of-interest definitions [21] that limit the application of the results in out-of-lab environments.



Figure 10: Label adaptation examples. For side profile views in the CHARLOTTE dataset only landmarks for visible parts of the face exist and additional positions on the forehead are marked. Label adaptation translates the three different landmark conventions we use for evaluation (bottom) into the CHARLOTTE convention (top).

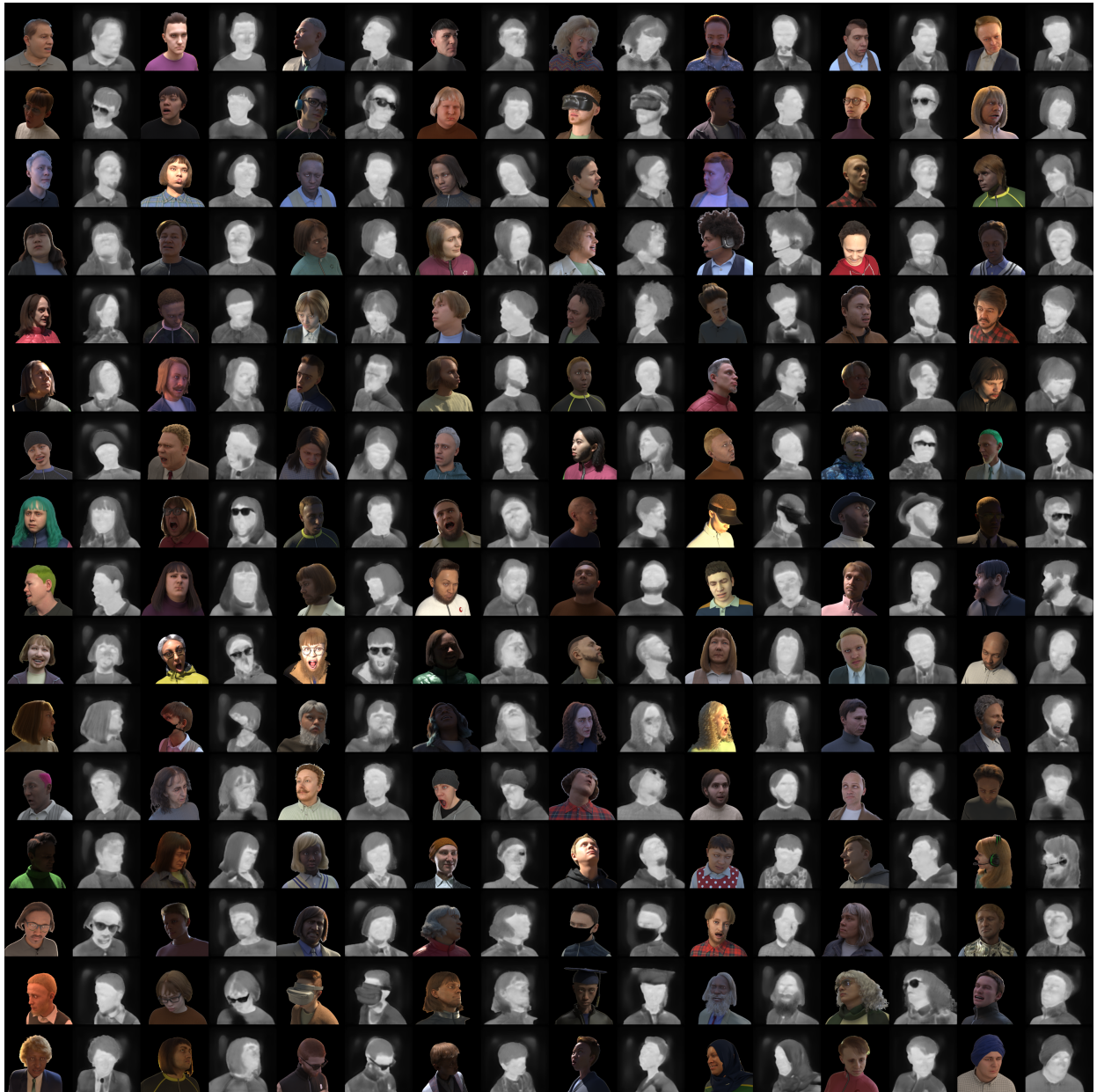


Figure 11: The first 128 FAKE (with removed background) and T-FAKE images with a random choice between the 'cold' and the 'warm' variant.



Figure 12: The sparse landmarks for the T-FAKE images in Fig. 11